Constraining ice fabric in a fast-flowing Antarctic ice stream using icequakes

S.-K. Kufner[1*†], J. Wookey[2], A. M. Brisbourne[1], C. M. Garcia[1], T. S. Hudson[3], J. M. Kendall[3], and A. M. Smith[1]

[1]British Antarctic Survey, Natural Environment Research Council, Cambridge, UK.

[2]University of Bristol, School of Earth Sciences, Bristol, UK.

[3]University of Oxford, Department of Earth Sciences, Oxford, UK.

* Corresponding author: Sofia-Katerina Kufner (sofia-katerina.kufner@kit.edu)

† Now at the Karlsruhe Institute of Technology, Geophysical Institute, Karlsruhe, Germany

Key Points:

- Split shear waves from basal microseismicity are used to invert for ice fabric.
- The preferred model has three depth layers of distinct fabric (0-400m depth: tilted cone, -1600m: thick girdle, -2200m: vertical cone).
- Anisotropic ice flow modelling with this model shows that viscosity varies with depth, direction and component of deformation.

Abstract

The crystal orientation fabric of glacier ice severely impacts its strength and flow. Crystal fabric is therefore an important consideration when modelling ice flow. Here, we show that shear wave splitting (SWS) of glacial microseismicity can be used to invert for seismic anisotropy and ice fabric at Rutford Ice Stream (RIS). RIS is a fast-flowing Antarctic ice stream, a setting crucial for informing flow models. We present >2000,000 SWS measurements from glacial microseismicity, registered at a 38-station seismic network located ~40 km upstream the grounding line. A representative subset of this data is inverted for ice fabric. Due to the character of SWS, which accumulates along the ray path, our method works best if additional information on the depth structure of the ice is available, which are radar measurements in our case. We find that the following three-layer model fits the data best: a broad vertical cone near the base of RIS (500 m thick), a thick vertical girdle, orientated perpendicular to flow, in the middle (1200 m thick) and a tilted cone fabric in the uppermost 400 m. Such a fabric causes a depth-dependent strength profile of the ice with the middle layer being ~3.5 times harder to deform along flow than across flow. At the same time, the middle layer is a factor ~16 softer to shear than to compression or extension along flow. If such a configuration is representative for fast-flowing ice streams, it would call for a more complex integration of viscosity in ice sheet models.

Plain Language Summary

We introduce a method to derive information on the ice viscosity of a >2 km thick Antarctic Ice Stream by using glacial microseismicity. When an external force is applied to ice, the individual ice crystals are rearranged in a specific configuration. Dependent on this configuration, the bulk ice is then harder or more easy to deform, dependent on the direction of applied force. This is behavior can be expressed through the viscosity tensor, which is an important parameter in ice sheet models.

At the same time, ice is highly anisotropic, meaning that the wave speed of seismic waves depends on the direction of propagation. We use a seismological method to measure this anisotropy. As different ice crystal configurations feature a characteristic anisotropy pattern we can then use these measurements to invert for the crystal configuration in the ice. Our results show that the crystal configuration varies with depth, which severely affects the ice stream's behavior upon deformation. Such an behavior is so far not included in most ice sheet models.

1 Introduction

Much of the uncertainty in current scenarios of future sea level rise originate from different predictions for the contribution of the West Antarctic Ice Sheet (IPCC, 2007). This contribution is mostly constrained by large-scale ice sheet models, which are designed to understand the ice sheet behavior in response to external forces (Graham et al., 2018). An essential part of such models are flow relations, which relate applied stress to the deformation in the ice. Stress modifies the internal structure of glacial ice through the alignment of individual anisotropic ice crystals into preferred crystal orientation fabric (e.g., Faria et al., 2014b). The internal crystal structure of ice, hereafter referred to as ice fabric, then influences the mechanical properties, and therefore ultimately the flow pattern of ice streams, as different types of ice fabric deform distinctly under stress (Alley, 1988). This is because the alignment of ice crystals happens by creeping along the c-axes of the hexagonal ice crystals (Duval et al., 1983). Depending on the applied forces, different types of ice fabric can develop. If ice crystals are subject to uniaxial compression, their c-axes orient into a cone-shaped distribution around the direction of applied stress, commonly referred to as 'cone' or 'cluster fabric' (Figure 1a). Uniaxial compression results in 'thick girdle fabric', where c-axes are oriented perpendicular to the compression axis (Figure 1b). A 'partial girdle' fabric may develop under a combination of pure and simple shear (Figure 1c) (Alley, 1988; Maurel et al., 2015). These different ice fabric types have a characteristic pattern of anisotropy (the variation of direction of mechanical properties, including seismic wave speed), which is different from single-crystal ice, and which varies dependent on the azimuth and on the incidence angle from which the fabric is sampled (Figure 1). Laboratory and field studies have shown that the anisotropy of ice significantly influences ice deformation and should therefore be incorporated into ice sheet models (Graham et al. (2018) and references therein). Knowledge of the present-day ice fabric is

therefore essential for predicting the future behavior of ice streams when using flow models (Azuma & Goto-Azuma, 1996).

Commonly, anisotropy is implemented in ice sheet models through a tensional relationship for bulk ice viscosity (Faria et al., 2014b; Gagliardini et al., 2009; Ma et al., 2010) or as a parameter, determined empirically from the surface stress filed (Budd et al., 2013; Graham et al., 2018). This is because direct observations of ice fabric from drilling or coring are mostly located near ice domes (Faria et al., 2014a, 2014b), where cone fabrics, which are vertically transverse isotropic, are common. However, recent measurements from Rutford ice stream (RIS), a fast-flowing West Antarctic ice stream, conducted using non-invasive geophysical methods, suggest that the mechanical properties of ice vary significantly laterally and with depth in such settings (E. C. Smith et al., 2017; T. M. Jordan, 2022). These results call for a more complex consideration of anisotropy in ice sheet models.

Non-invasive geophysical methods, like active and passive seismic imaging, or radar sounding (e.g., Picotti et al., 2015; E. C. Smith et al., 2017; T. M. Jordan, 2022), make use of the fact that the different ice fabric types feature different patterns of anisotropy (the variation of elastic or electromagnetic wave speed with direction of propagation). Compared to direct observations, such methods are less time and cost intensive in the field but result in some ambiguity in the ice fabric inferred. The radar method used by Jordan et al. (2022), for instance, is only sensitive to crystallographic preferred orientation in the horizontal plane. Thus, only the difference of the horizontal eigenvalues of the fabric-orientation tensor can be determined. By contrast, using shear wave splitting (SWS) of seismic waves, Smith et al. (2017) were able determine two fabric types that seem to be present in the ice of RIS. However, they could not resolve the spatial location of these different fabric types as SWS integrates along the entire ray path of seismic waves (Silver & Savage, 1994), Here, we aim to obtain a more comprehensive picture of ice fabric at RIS by making use of the advantages of different geophysical methods. First, we generate SWS measurements similar to Smith et al. (2017). We then use the seismic waveforms to invert for ice fabric, implementing a multiple-layer inversion scheme (Wookey, 2012). We show that the problem of unknown spatial location of different fabric types can be overcome by using depth-information from radar measurements (T. M. Jordan, 2022) as prior constraints for the inversion. This approach allows us to narrow down the depth range of different ice fabric types and to calculate the full viscosity tensor for these depth domains. Both are essential for the transfer of geophysical results to the parameter space used in ice sheet modelling.

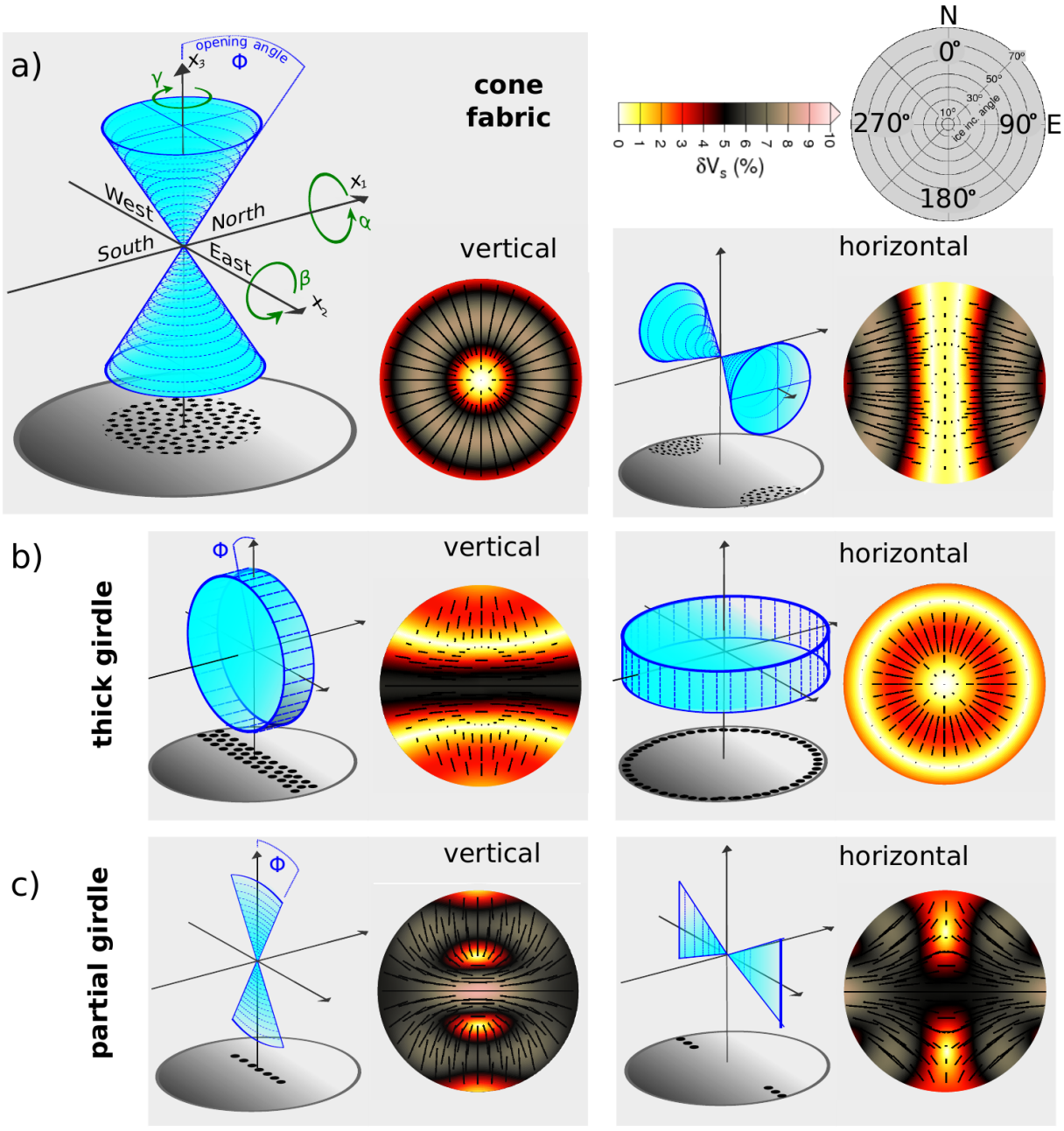

Figure 1: Schematic plots of ice fabric properties and expected SWS pattern on a polar diagram. Fabric figures are adapted from Maurel et al. (2015) *and Smith et al.* (2017)*. In the schematic diagrams, the envelope of c-axes is highlighted*

in blue, while black circles at the base of the plot show the c-axes distribution on an upper hemispheric plot. Θ describes the opening angle of the envelope, while , and are the rotation angles around the coordinate axes, which are used in the inversion (see Section 4). Insets show upper hemisphere polar diagrams of the percentage of shear wave anisotropy (V_S), expected for the different fabric types. The associated coordinate system is given in the top right. North refers to an azimuth of 0°. a) Vertical (=0°; left) and horizontal (=90°; right) cluster fabric with Θ=30°. b) Vertical (=0°; left) and horizontal (=90°; right) thick girdle fabric with Θ=15°. c) Vertical (=0°; left) and horizontal (=90°; right) partial girdle fabric with Θ=15°.

2 Site Description and Dataset

Our study area is in a central section of Rutford Ice Stream (RIS), 40 km upstream from the grounding line (Figure 2). RIS flows approximately southward into the Filchner-Ronne Ice Shelf with a velocity of 375 m/a (Adalgeirsdóttir et al., 2008). Beneath the 8 x 8 km 38-station seismic array (Figure 2), which was deployed as part of the BEAMISH project (A. M. Smith et al., 2020), the ice thickness is approximately 2.2 km (King et al., 2016). Ice flow direction, determined from the GPS instruments attached to our seismometers, is 148° relative to north. Due to the movement of the ice over its bed, many microearthquakes (local magnitude smaller than –0.3) are created in this section of RIS (Kufner et al., 2021; E. C. Smith et al., 2015). These events are characterized by relatively simple waveforms, featuring an impulsive P onset with 10 to 200 Hz frequency followed by a shear wave with frequencies between 30 and 100 Hz (Kufner et al., 2021). In cases where the source polarization is not parallel to the ice fabric symmetry axes, the shear waves of these events are split into two orthogonally polarized quasi shear waves (Figure 3), which is known as shear wave splitting (SWS). The quasi shear waves travel at different speeds, dependent on the ray path orientation relative to the ice fabric. The delay time (dt) between the two shear wave components is an indicator of the strength of seismic anisotropy along the ray path, the polarization direction of the quasi-shear waves depends on the symmetry of anisotropy along the ray path (e.g., Silver & Chan (1991), Savage (1999), Teanby (2004)). Here, we measure dt and Φ (the polarization direction of the faster of the two quasi-shear waves) from 69,629 microearthquakes (Figure 2) recorded at 38 seismometers during approximately three months from November 2018 to February 2019, using the automated SWS splitting software MFAST (M. K. Savage et al., 2010). Waveforms were recorded with a sampling frequency of 1000 Hz by Reftek RT-130 data loggers with 4.5 Hz three-component geophones (see Kufner et al. (2021) for details). The event-station pairs used in this study have been selected from the event catalog of Kufner et al. (2021), based on the availability of both P- and S-picks and a focal mechanism solution. The latter allowed us to compare the slip vector from focal mechanisms and SWS as an additional quality control.

Previously, Smith et al. (2017) used a 10-station seismic array at a similar location to detect SWS of 5,951 event-station pairs and to invert the SWS pa-

rameters for ice fabric. Smith et al. (2017) tested combinations of two different fabric types (hereafter referred to as 'mixed' fabric) as potential candidates that could create the observed SWS pattern. They concluded that the anisotropy observed in their SWS data could be due to a horizontal partial girdle, orientated with a symmetry axis perpendicular to ice flow, combined with a cluster fabric with a relatively large opening angle of 73° (see Figure 1 for a schematic sketch of different ice fabric geometries). However, Smith et al. (2017) noted that the inversion for mixed fabric is unconstrained, as SWS samples the anisotropy along the entire ray path. Thus, the two fabric types may be spatially separated in the ice stream. Their observations indicate a region of mostly extension and horizontal confinement (expressed through the horizontal partial girdle) in combination with a weakly anisotropic region (expressed through the cone with large opening angle). The weakly anisotropic region could either be the firn layer, or a deeper region with thin layering, which would weaken the bulk anisotropy. It was later noted that a horizontal partial girdle fabric was never observed directly in boreholes (Lutz et al., 2020). Thus, although this model explains the SWS data, it remains a topic of discussion if this configuration is a realistic scenario in a fast-flowing ice stream.

A later radar study by Jordan et al. (2022) delineated the shallow depth structure of ice fabric at RIS in more detail. At a site, overlapping with the seismic array used in this study (site A1 in Jordan et al. (2022); see Figure 2), the azimuthal anisotropy was observed to change spatially in the upper 400 m with a symmetry axis within ±20° of the current flow direction of RIS. In the upper ~150 m, anisotropy is closely orientated along the surface strain field, whereas the symmetry axes in a deeper (150-400 m) layer appeared rotated by ~20° in a clockwise direction relative to shallower ice. Surface strain rate was calculated by Jordan et al. (2022) from geodetic data. The section of RIS in which our study region is located, is characterized by small along-flow compression and small lateral extension relative to flow. By contrast, further upstream, along-flow extension is more dominant. Thus, Jordan et al. (2022) suggested that the ice fabric configuration they measure at site A1 might arise as the fabric is created further upstream and then buried and advected. However, due to the radar survey method, only the symmetry axes of the vertical anisotropy and the intensity can be modelled. For instance, a thick girdle or a horizontally orientated cone fabric would yield the same pattern in the radar data. Deeper (~400-1600 m depth), the method used by Jordan et al. (2022) did not have sufficient coherence in the data to detect the axes of anisotropy. Notably, coherence does improve deeper than 1600 m and a region with azimuthally invariant anisotropy was inferred. This suggests either isotropic ice or a fabric with a vertical axis of symmetry. Furthermore, the sharp recovery of coherence could mean that the ice fabric shallower than 1600 is different from that in the deepest ice.

The combination of results from these two studies suggests that the ice fabric of RIS is depth-dependent. Potentially three or more layers of distinct ice fabric might be sharply separated from each other. Intensity and fabric types in these

layers are narrowed down through the studies of Smith et al. (2017) and Jordan et al. (2022) but could not be uniquely defined. In this study we extend the seismic anisotropy study of Smith et al. (2017), making use of the results from Jordan et al. (2022) to obtain a more comprehensive picture of the variation of ice fabric with depth, which then allows to calculate the full fabric orientation tensor and ice viscosity.

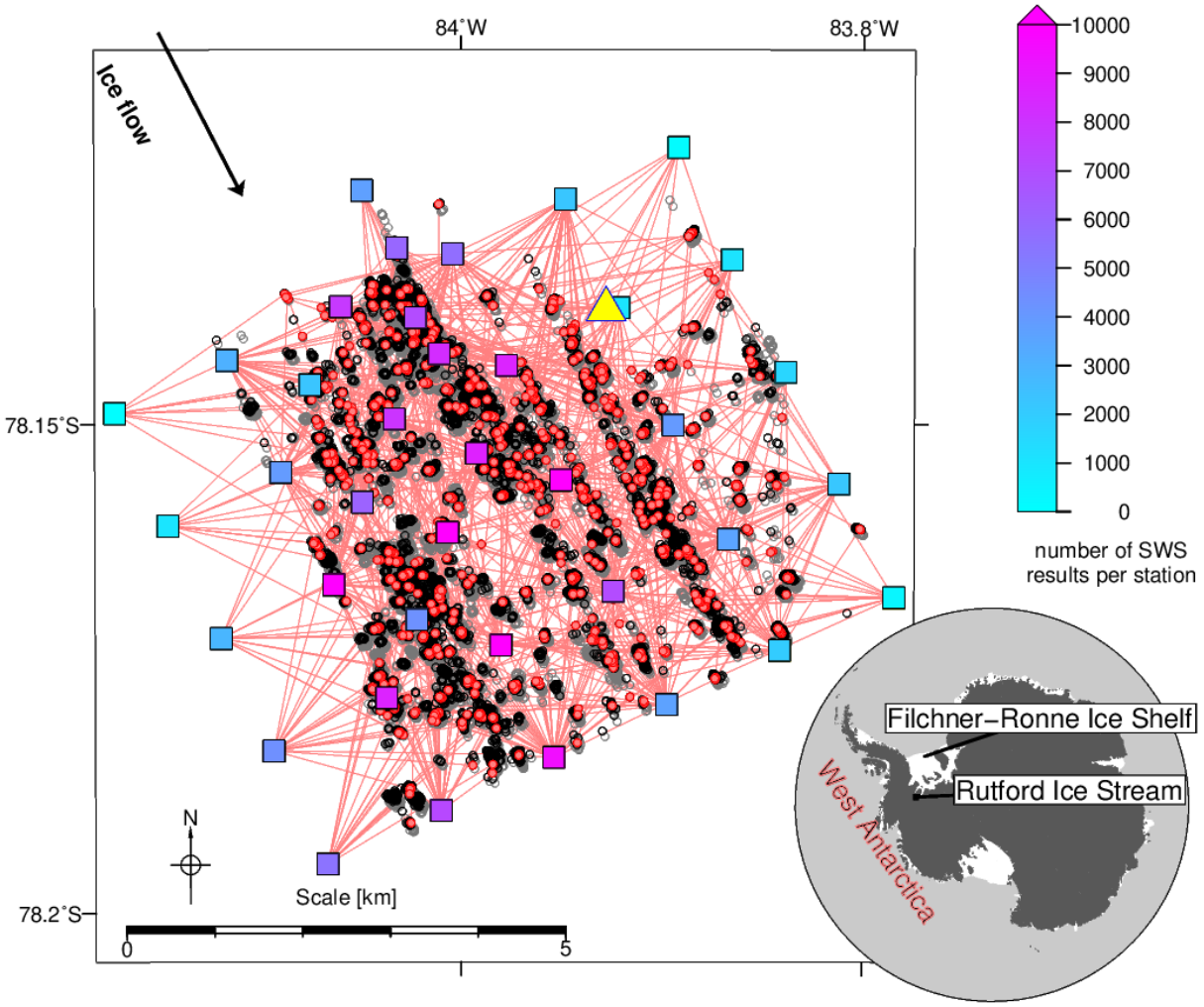

Figure 2: Geographic setting of Rutford Ice Stream, location of seismic array and earthquake locations used for SWS analysis. The yellow triangle shows the radar survey site of Jordan et al. (2022)*, which data are used to design input models for inversion. Stations (squares) are color coded according to the number of good SWS results registered at this station. Gray circles are all microearthquakes on which waveforms SWS was performed (167,262 events), black circles are those*

with good SWS results (69,629 events), red circles and light red ray paths highlight those selected for ice fabric inversion (1090 events). Inset shows the location of Rutford Ice Stream relative to the Antarctic continent.

3 Shear-wave Splitting

3.1 Method and Data Processing

To calculate SWS parameters from our waveform data, horizontal seismograms are filtered between 8 and 125 Hz, using a two-pole Butterworth filter, and downsampled from 1000 to 500 Hz. This further increases the number of high-quality splitting measurements at larger epicentral distances, while leaving results at smaller epicentral distances unchanged compared to the unfiltered case. Downsampling increases processing speed, while preserving the frequencies of interest. In the following, we refer to this pre-processed data as 'unfiltered'.

We use the MFAST software (M. K. Savage et al., 2010) for SWS analysis. MFAST implements a minimum eigenvalue analysis algorithm (Silver & Chan, 1991) to calculate SWS in multiple time windows around a specified S-wave onset. For each of these measurement windows, inverse splitting parameters (i.e., a rotation to the fast-slow reference frame, followed by a time-shift) are applied to the horizontal waveforms. This aims to find the combination of splitting parameters that minimizes the quotient of the two eigenvalues (2/ 1)* 2 (referred to as 2' in the following) of the covariance matrix of the two horizontal traces. During this calculation, the mean of the two traces is removed, which stabilizes the solution. In addition to the two splitting parameters (Φ and dt), a by-product of the minimum eigenvalue method is the initial polarization direction (which depends on the source moment tensor). As SWS measurements can depend on the chosen analysis window, a cluster analysis method is then implemented on the splitting results from a number of differing-length individual measurement windows to find the most stable set of splitting parameters (see Teanby et al. (2004) for more details). In MFAST, the start and end point of the measurement windows are variable, dependent on an event's dominant frequency. Constraint is the measured Φ and dt is estimated using an F-test (Silver & Chan, 1991; Walsh et al., 2013).

Here, we first calculate the signal-to-noise ratio of all candidate events based on time windows 0.1 s prior to and after the S-onset on the horizontal components and require a minimum signal-to-noise ratio of two for further analysis. In the case that half the S-P time is smaller than 0.1 s, we restrict the noise window to half the S-P time. We search Φ from 0 to 180° and dt from 0 to 0.1 s, based on trial runs with the largest possible dt. We find our SWS results to be remarkably stable across different analysis windows as glacial microseismicity at RIS features generally simpler waveforms than tectonic earthquakes. We therefore use only two analysis time windows prior and four after the S-onset. Only when no stable cluster could be found is the number of measurement windows prior to the S-onset increased to six. In addition, the same restriction criteria for the signal-to-noise analysis is implemented, so that P wave energy is never included

in the analysis. For our final set of SWS results, measurement windows range from 0.013 to 1.25s prior and 0.050 to 1.01s after the S-onset, while the mean dominant frequency is 29 Hz. After SWS analysis, we obtain 705,441 sets of splitting parameters from the initial 989,686 event-station pairs. Depending on the stability of the cluster and the error range of the final splitting parameters, MFAST adds a quality grade to the data (see details in Savage et al. (2010)). Here, we use these grades for reference, but additionally apply data-set specific quality restrictions to our final splitting measurements. These criteria have been defined based on visual inspection of a subset of results. We require the calculated error in Φ to be smaller than 15° and the error in dt to be smaller than 0.005 s. Furthermore, a quality criterion is defined based on the amplitude ratio on the component, which is normal to the initial source polarization direction, before and after correcting for splitting (stc/sto) and based on the cross-correlation coefficient of fast and slow shear wave after correcting for splitting (coeff). We set: stc/sto <0.6 and coeff>0.7 or stc/sto <0.5 and coeff>0.6 or stc/sto <0.45 and coeff>0.5.

Figure 3 shows examples of two SWS measurements, one high quality result (Figure 3a) and a second example (Figure 3b) of lower quality. SWS is successfully measured and removed in the first case. By contrast, the cross-correlation coefficient between corrected fast and slow component in the second case is smaller and the maximum in the misfit surface of 1/ 2' is less pronounced. Notably, the lower quality of the second example is not due to noise but rather due to the structure of the waveforms themselves.

To test if the SWS results depend on filter frequency, we recalculate splitting parameters at different frequencies for one day of data (1st of January 2019; ~5,800 station-event pairs). We test the frequency bands 20-40 Hz and 30-90 Hz and find that many results (between 67% and 84%) are similar within the standard errors of the different measurements. The difference in results between the filters is mostly in dt due to cycle skipping as the finer-scale structure of the waveforms is removed in the filtered waveforms (see details in Supplementary Figures S1 and S2). This highlights the importance of conducting the SWS measurements with the broadband waveforms, at least for this specific dataset. Measurements where no cycle skipping occurs do not show a variation of splitting parameters with filter frequency and a high percentage (93% and 95% for dt in the 30-90 Hz and 20-40 Hz range, respectively, and 96% and 74% for Φ in the 30-90 Hz and 20-40 Hz range, respectively) are similar within the uncertainty range of the individual measurements (Supplementary Figures S1 c and d). This agrees with Smith et al. (2017), who also did not find evidence of frequency dependence in their results.

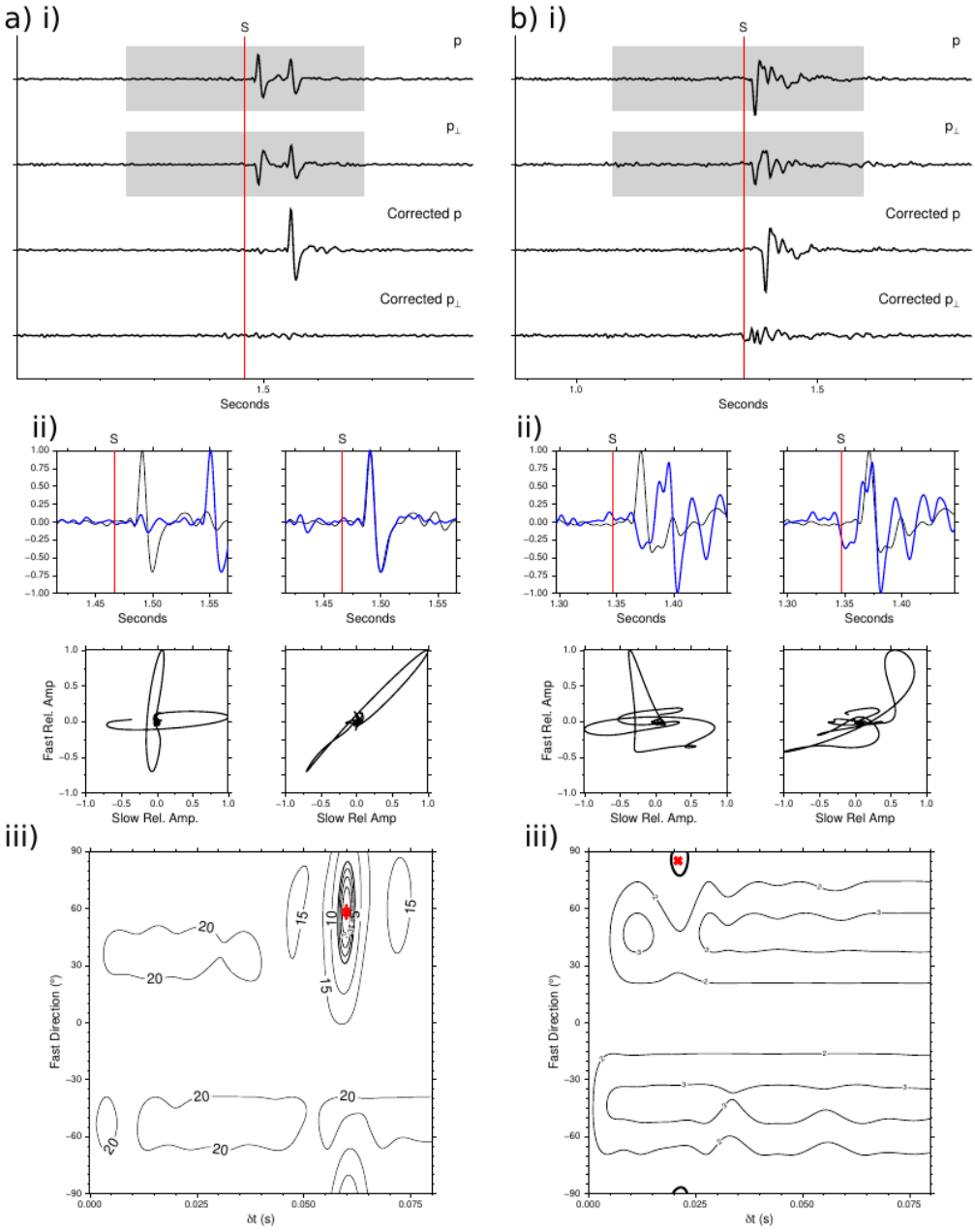

Figure 3: Examples for SWS results. Subfigures i show the horizontal traces rotated into (p) and perpendicular (p) to the polarization direction, which is determined in MFAST together with the splitting parameters. 'Corrected' refers to traces rotated into and perpendicular to the polarization direction after correction for the optimum anisotropy parameters. Amplitudes of the traces are

normed. The splitting window is highlighted in gray, the location of the S-pick in red. Time is relative to the start of the data trace. For an optimum set of splitting parameters, the energy on 'corrected p ' is minimized. Subfigures ii show waveforms (top) and particle motion (bottom) of the fast and slow components. Original fast and slow waveforms are plotted in the two left panels, while for anisotropy corrected waveforms are plotted in the two right panels. As in (i), the red line represents S-pick. Subfigures iii show the misfit surface of 2'. The 95% confidence interval corresponds to the bold "1" contour. Other contours demarcate multiples of the 95% confidence interval. Contours are only shown until the tenth multiple. The optimal splitting parameters are highlighted as red cross. a) Example for high quality results, representative for events with near vertical incidence angle (event date time: 2019/021/01 01:01:17; magnitude: -1.15; epicentral distance: 0.14 km; azimuth: 137°; incidence angle: 5°). b) Example for a result with worse quality. For instance, the final SWS parameter do not completely remove the energy on the 'corrected p ' component (event date time: 2019/01/01 00:18:09; magnitude: -0.79; epicentral distance: 1.72 km; azimuth: 352°; incidence angle: 26°). Such results mostly occur at larger incidence angles but not for all azimuths.

3.2 Shear-wave Splitting Results

We obtained 202,651 SWS results (average/min./max. 5,333/74/13,677 results per station; average/min./max. 3/1/16 results per event). The dataset is available online (Kufner et al., 2022). The distribution of these results in map view (Figure 2) is representative of the available event and station distribution (i.e., more good splitting results in the center of the network, due to more available rays and microearthquakes). Results are presented in Figures 4 on a polar plot in upper hemispheric projection albeit many individual SWS overlap in this representation. Therefore, we additionally calculated bin-wise averages (Figure 5), which helps identify trends in the data. Here, and in the following analysis, we use the percentage of anisotropy (V_S) – the percentage of shear wave variation from the average isotropic velocity (1944 m s^{-1}) – instead of dt when visualizing SWS results. V_S is calculated as 100*(1944 m s^{-1} *dt)/(ray length). The advantage of V_S is normalized with respect to ray-path length, compared to dt.

Our SWS results include rays from all azimuthal directions, 0.01 to 4.9 km epicentral distance and incidence angles from 1.2 to 42.9° (calculated from a layered velocity model with a 100 m thick firn layer overlaying glacial ice, as used by Kufner et al. (2021)). Few of the incidence angles therefore exceed 35°. For larger incidence angles, P-wave conversions might bias the SWS results (Crampin & Lovell, 1991; Paulssen, 2004). However, as the general trend of the SWS results is consistent between 30° and 43°, this set of results seems unaffected by such a bias.

The initial shear wave polarization determined from SWS (average of 154°) and the slip vectors from focal mechanisms, determined from the fault plane solutions of Kufner et al. (2021) (average of 160°), are comparable (Figure 4c). As

these two measures are determined independently, their similarity validates the quality of the SWS parameters. Lastly, Figures 5b and c show the standard deviation ( ) of splitting parameters from the bin-wise averaged values. is generally small (average of V_S: 0.49%; average of Φ: 15.7°), which suggests a general consistency in the results throughout the study region.

Average V_S is 2.2% (min/max.: 0.16/6.6%), which is calculated from split times between 0.0025 and 0.084 s (average: 0.029 s; average error: 0.00038 s). Average Φ is 61° (average error: 3.8°) but SWS parameters strongly vary with azimuth and with incidence angle (Figures 4 and 5). Φ is dominantly perpendicular to ice flow direction. The highest V_S values (up to 6.6%) are measured for incidence angles smaller than ~15° (highlighted as feature f1/f1x in Figure 5a). At incidence angles between ~15° and ~30°, V_S is smaller and alternates in magnitude dependent on azimuth. The smallest V_S values (<1%) are measured in four domains at ~60°, ~150°, ~240° and ~330° (highlighted as features f2 in Figure 5a). These domains are oriented parallel and perpendicular to the ice flow direction at the surface. For the other azimuthal orientations, V_S is larger (between 2 and 4%) but Φ is rotated by approximately 20° relative to the direction perpendicular to ice flow (highlighted as feature f3/f3x in Figure 4a). For the largest incidence angles (>30°), the variations in intensity of V_S are less intense, and V_S is larger (between 2 and 4%) for all azimuths (highlighted as feature f4/f4x in Figure 5a).

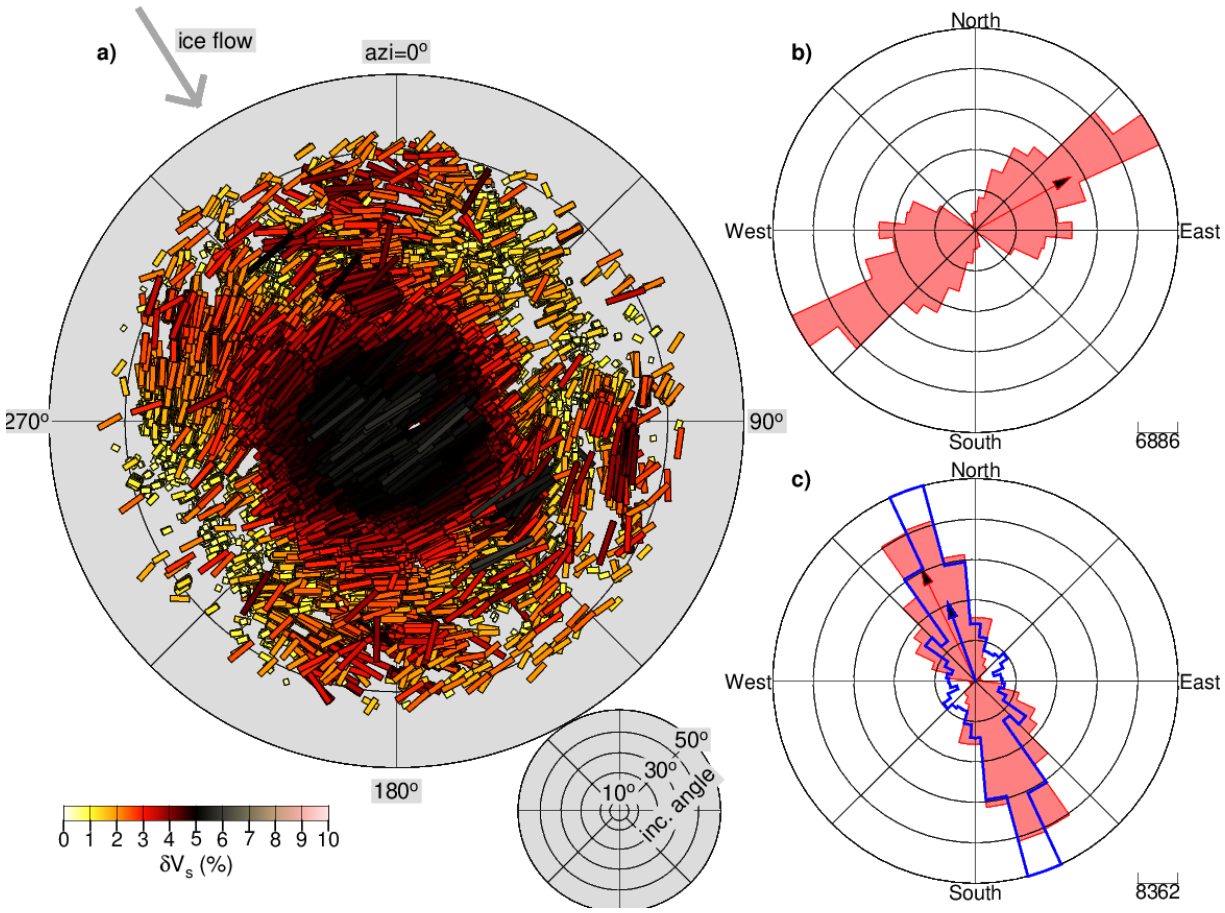

Figure 4: a) Upper hemisphere plot of SWS measurements. Direction of bars indicates Φ, length and color the percentage of anisotropy (V_S). Azimuth from event to station (azi) is plotted clockwise from north, incidence angles of the rays (inc. angles) as shown in the inset plot. Ice flow direction is drawn as gray arrow. b) Rose diagram of Φ, plotted in 10° bins. Arrow represents the average value. c) Rose diagram comparing initial S-wave polarization, determined from SWS (red) and slip vectors (Kufner et al., 2021)*, determined from the events' focal mechanisms (blue). Arrows represent average values.*

In addition to these large-scale trends, we resolve a modulation of the splitting results relative to the symmetry axis of ice flow direction: First, the SWS measurements at small incidence angles are not purely perpendicular to flow but exhibits a small rotation towards this symmetry axis in the south-west (at an azimuth of ~240°; highlighted as feature f1x in Figure 5a). Next, we observe a slight asymmetry in the intensity of the f3 domains: larger V_S is observed in the south-west (at azimuths of ~285 and ~195°; highlighted as feature f3x in

Figure 5a). Lastly, for the largest incidence angles (>30°), we observe larger V_S in the south-west (highlighted as feature f4x in Figure 5a) compared to the north-east. These patterns in the data remain stable, independent of whether Null measurements (15% of all measurements, for which the difference between Φ and initial polarization is <20°) are included or excluded from the polar plots (Figure S4).

Based on the averaged bins (Figure 5), we investigate the dataset for temporal and spatial changes in splitting parameters (Supplementary Section S1 and Figure S5). Few bins (<5%; from visual inspections) show a weak variation of V_S in map view but these variations are not systematic across the different bins (e.g. one bin exhibits larger V_S to the north-east whereas another bin exhibits larger V_S to the south-west of the network). Moreover, variations from measurements uncertainties are larger than these trends. Thus, we conclude that the variation of splitting parameters in our study region is predominantly dependent on incidence angle and azimuth. This is in accordance with the findings of Smith et al. (2017) and suggests that potential spatial or temporal changes of ice properties are within the uncertainty of the SWS method used here.

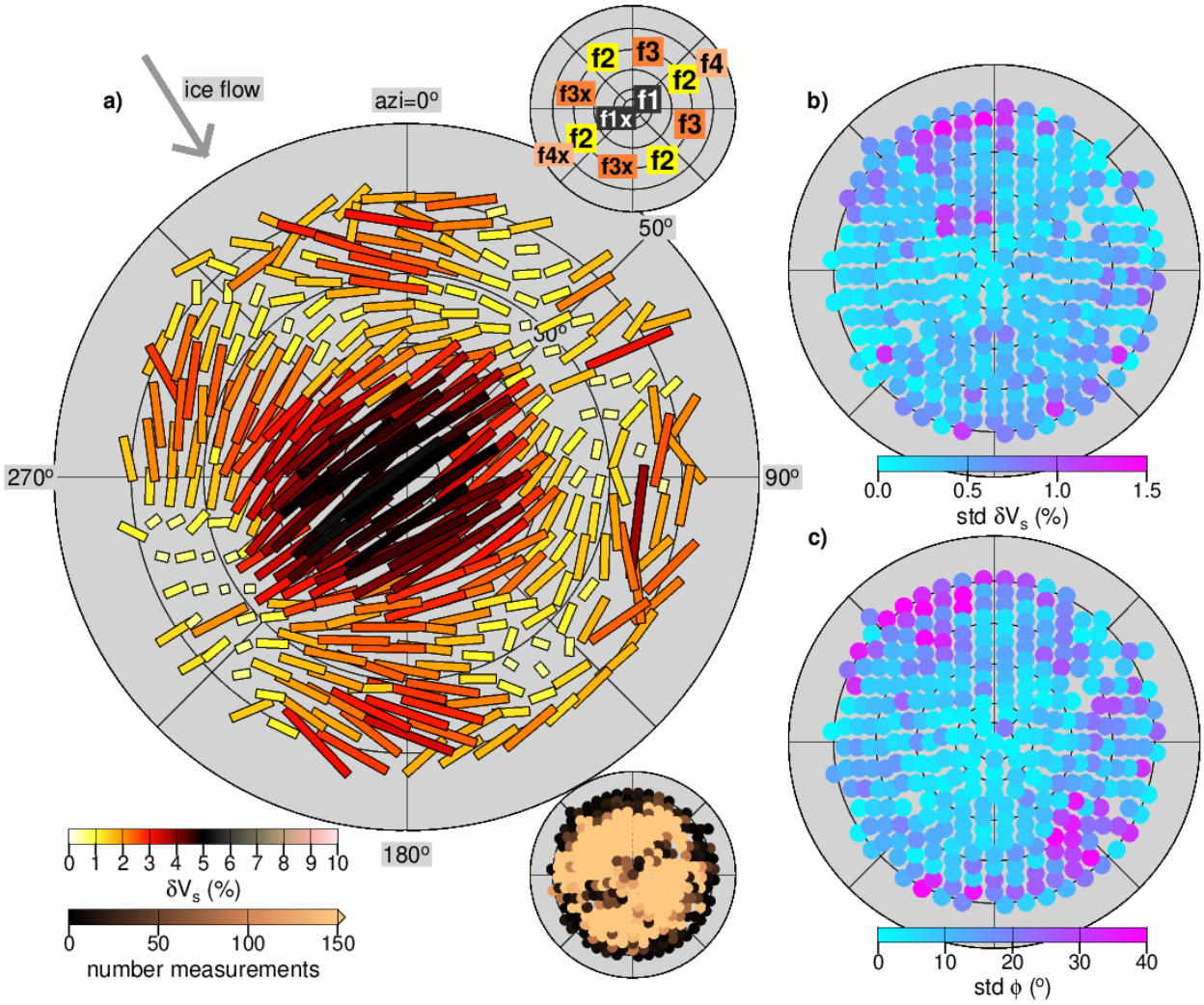

Figure 5: a) Upper hemisphere plot of averaged SWS measurements. Averaging is performed on bins of 3° incident angle. Azimuthal bins are adjusted dependent on incidence angle, with one bin at an incidence angle of 0° and 48° bins at an incidence angle of 40°. In each bin, weighted averages are calculated based on the events' signal-to-noise ratio (see Figure S3 for the weighting function) and only splitting results with ACl quality from MFAST are included. Bottom inset shows number of measurements included in each bin. The color scale is clipped to highlight bins with few measurements. The maximum number of measurements per bin is 5513, the mean is 531. Top inset shows labels of the main features in the data as discussed in Section 3.2. b) and c) Upper hemisphere plot of standard deviation (std) of V_S and Φ per bin.

4 Inversion for Ice Fabric

4.1 Inversion Method and Input Data

We use the multiple layer SWS inversion scheme introduced by Wookey (2012) to determine which ice fabric would yield the seismic anisotropy pattern in Figures 4 and 5. Within the inversion scheme, the subsurface is separated into several depth domains, for which a specific ice fabric is defined. For each of these depth domains, several ice fabric-specific parameters are varied over a predefined range of values. In each layer, and for all combinations of ice fabric-specific parameters, splitting parameters (Φ and dt) are then calculated based on the anisotropic tensors of the fabric and the geometry of different input ray paths (incidence angle and azimuth). Elastic tensors of ice fabric are defined according to Maurel et al. (2015). The splitting parameters for each depth domain are then applied sequentially to the waveforms in reverse order (starting from the surface) within the measurement window that had been used for the SWS measurements. After sequentially applying the splitting parameters of all depth domains, 2' is calculated from the resulting waveforms similar to MFAST. The algorithm then searches for the input set of fabric-specific parameters that maximizes the inverse of the sum of 2' of all input waveforms ($1/\Sigma$ 2'). This search for the best model is conducted via a nonlinear inversion scheme (Markov Chain Monte-Carlo using a Metropolis-Hastings algorithm, see Wookey, (2012) for more details on the method). Here, we use 200,000 test models in the algorithm. Test runs with more models did not yield different results. Modifications in the inversion scheme applied here, compared to the original version of Wookey (2012), include removing the mean of the waveforms when calculating the covariance matrix, using 2' instead of 2, and adapting the inversion scheme for ice fabric through implementing the elastic tensors. The latter is attributed to the specific setting of a glacier, the former modification yielded more stable results in trial inversion runs and was adapted from MFAST.

We determine the final model from the combination of ice fabric-specific values that maximizes $1/\Sigma$ 2'. If several models yield equally high $1/\Sigma$ 2', we used the mean from all the best models. The uncertainty of each ice fabric-specific parameter is defined from the range of all models that lie in the upper 20% of $1/\Sigma$ 2'. We chose this value as it yielded comparable uncertainty bounds to those derived for SWS in MFAST, when running the inversion for one ray only.

The main advantage of this inversion method is that it operates directly on the waveforms. Therefore, bias that could be introduced by fitting a fabric model to the final SWS results are prevented. However, as each input waveform contributes equally to the final solution, an equal distribution of input data throughout the entire range of incidence angles and azimuths is important. Therefore, we use only a representative subset of all waveforms, for which we had calculated SWS results, as input for inversion. To ensure a representative distribution of rays throughout the study region, we separate the region into six lateral spatial domains, with the separation lines arranged parallel and perpendicular to ice flow direction. For each of these domains, we choose a subset of available waveforms based on the averaged SWS results (Figure 5). For each

spatial domain and for each of the averaged incidence angle-azimuth bins, only the best station-event pair is chosen. 'Best', here refers to the event-station pair with the largest cross-correlation coefficient of the corrected and rotated waveforms and the smallest uncertainty in Φ and V_S. In addition, only events for which the cross-correlation coefficient is larger than 0.5 and the uncertainty in Φ and V_S is smaller than 10° and 0.001%, respectively, are included. Lastly, only events from incidence angle-azimuth bins for which the standard deviations of Φ and V_S are smaller than 30° and 1.2% are included. These criteria ensure that the event-station pairs used for inversion are truly representative of the entire dataset. The final dataset then consists of 1,216 event-station pairs (Figure 2a; also shown in Figure S6 in more detail).

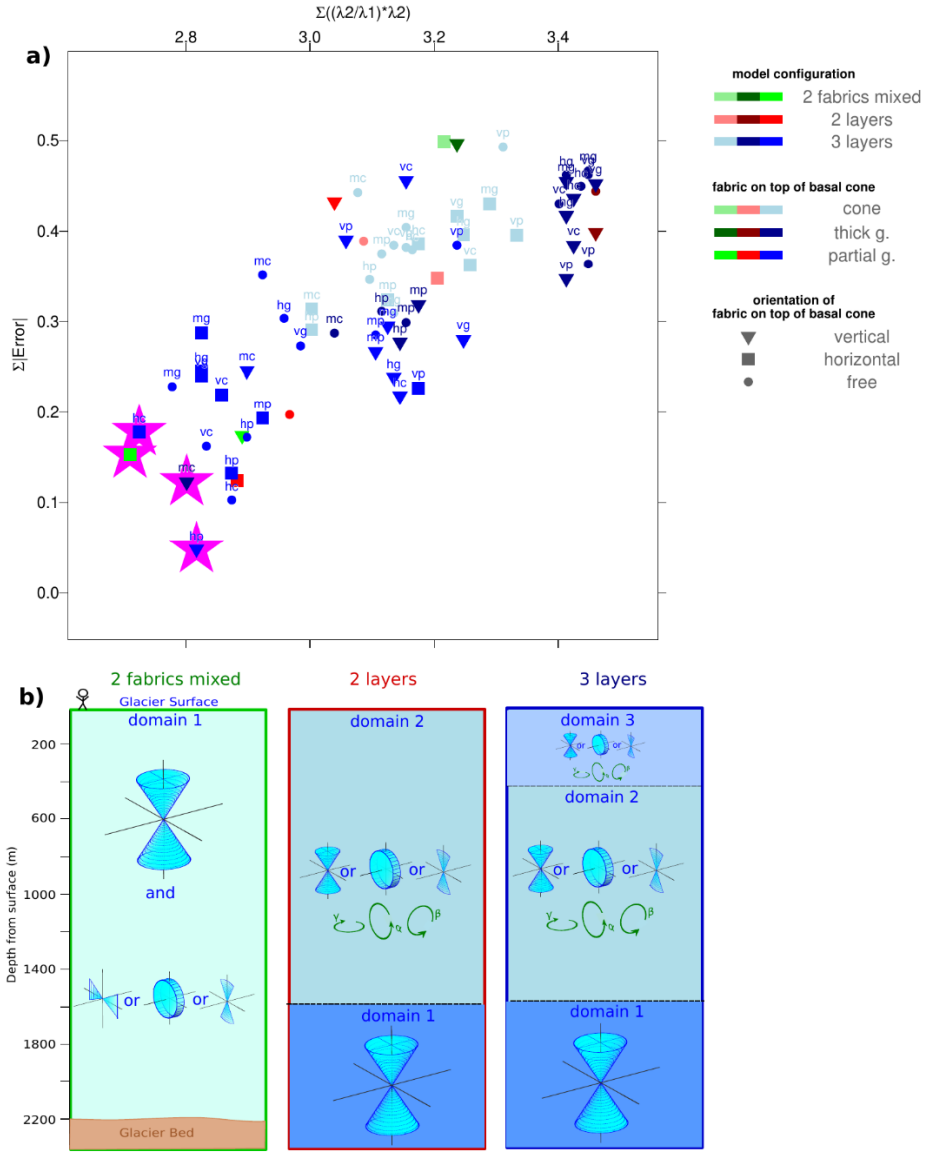

Figure 6: a) Comparison of inversion results. The best models feature small Σ 2' and a small normalized uncertainty of all individual parameters (Σerror) and are highlighted in purple. Plot colors, symbols and texts specifies the different models: Green, red and blue shaded symbols refer to models with two fabrics mixed (a vertical cone and one other fabric type), two-layer and three-layer models. The two- and three-layer models always feature a vertical cone in the bottom layer. The intensity of the plotted symbols refers to the fabric on top of the basal cone while the symbol refers to the orientation of the fabric. For the

three-layer models, the letters on top of the symbols specify the fabric type of the third layer (h/v/m p = horizontal/vertical/tilted partial girdle, h/v/m g = horizontal/vertical/tilted thick girdle, h/v/m c = horizontal/vertical/tilted cone). b) Schematic plot illustrating model geometries and ice fabric combinations tested in the inversion. Model geometry is inspired from the radar results of Jordan et al. (2022). *See Section 4.2 for a detailed explanation of the model setup.*

4.2 Model Setup

Figure 1 shows SWS parameters expected for different ice fabric types, which are either observed in ice cores or suggested previously for RIS. Comparing these patterns to Figures 4 and 5, it is obvious that none of these fabric types alone can explain the SWS measurements. Depth discrimination of anisotropy is a challenge, as SWS is accumulated along the entire ray path, and as all microearthquakes are located at the same depth. We overcome this limitation by making use of the radar results of Jordan et al. (2022) to predefine the layer structure for the inversion.

Jordan et al. (2022) resolve horizontally anisotropic fabric in the upper 400 m of RIS. At greater depth, coherency in their data decreases sharply but recovers at 1600 m depth, where they observe a fabric type which is horizontally isotropic. Based on these results, we define a three-layer model (Figure 6b): In the upper two layers (surface to 400 m depth and 400 to 1600 m depth), we test all likely fabric types (cone, thick girdle, and partial girdle). For each fabric type we run three different models: during two model runs, the fabric is fixed to be either vertical (or =0°; see Figure 1 for details on fabric geometry) or horizontal (or =90°). In the third run, we invert for or as well. Theoretically, this third model included the case of vertically or horizontally orientated fabric. However, predefining the fabric orientation reduced the number of free parameters, stabilizing the solution. In all model runs, we additionally invert for the opening angles of the fabric and , which is the rotation of the fabric relative to north. The separation of the upper 1600 m into two layers is based on the assumption that the sharp drop in coherency of radar results may arise from a change in ice fabric. We also include the case that the ice fabric remained stable by inverting for two-layer models in which the upper two layers are combined (Figure 6b). In the lowermost layer (1600 m depth to glacial bed at approx. 2200 m), we predefine a vertical cone fabric of unknown opening angle, as Jordan et al. (2022) observe a fabric with a vertical symmetry axis at this depth. One extreme case of this fabric could be an opening angle of 90°, which is equivalent to isotropic ice.

In addition to these three- and two-layer models, we invert for 'mixed'-fabric models like Smith et al. (2017). The 'mixed' fabric models are designed to compare our inversion approach to Smith et al. (2017) and always include a vertical cone and either a vertical thick girdle, a horizontal partial girdle or a vertical partial girdle. We invert for the opening angles of these fabrics, their mixing percentage and for the rotation of the girdle fabrics relative to north. 'Mixing' of the two fabrics is calculated through Voigt-Reuss-Hill averaging.

Lastly, we run sensitivity tests for the models that yielded the best results after the two-, three-layer and 'mixed' model inversions, aiming to investigate how much the final solutions depends on the predefined input constraints. Specifically, we vary the depth of the input model layers (from 0.2 km to 0.6 km depth for the uppermost layer and 1.4 km to 1.6 km depth for the middle layer). This minimizes any subjectivity in the interpretation of layer depth from radar measurements. In addition, we run further three- and two-layer models, placing the vertical cone fabric in the middle layer or leaving it out, aiming to determine the dependence of the solution on the layer sequence and the presence of a vertical cone fabric.

It should be noted that we refrained from including more than three depth domains in the inversion. Test runs showed that solutions for four-layer models, in which the uppermost layer was split into two 200 m thick layers, featured generally very large errors. This suggests that layers thinner or equal to 200 m may be too thin to be described adequately by the inversion method used here.

4.3 Inversion Results

To qualitatively compare all models, we plot Σ 2' versus the summed and normed uncertainty of all individual parameters (expressed as Σerror in the following) used in an inversion (Figure 6). The best models are expected to have small Σ 2' and small Σerror. The smallest Σ 2' value obtained from inversion is 2.71, which corresponds to a reduction of 23% relative to the uncorrected data (Σ 2'=3.53). It is worth bearing in mind that the results presented in Figures 6 include models with a different number of inversion parameters. However, comparing the number of free parameters with Σ 2' shows no direct correlation (Figure S7), suggesting that much of the variations illustrated in Figures 6 results from the characteristics of input models and not from the different number of free parameters.

Figure 6 illustrates that neither two-layer models nor three-layer models that feature a cone fabric in the middle layer can explain SWS to a satisfying extent. The two-layer models allow too little flexibility to capture finer scale trends in the data. A cone fabric, even when oriented horizontally, cannot account for the large V_S at small incidence angles. Four models yield comparably good results (highlighted in Figure 6a, details of these models are given in Figures 7-9 and Table S1). Interestingly, these models are composed of different fabrics (Figure 7). One of them is a 'mixed' model (Figure 7a), composed of a vertical cone and a horizontal partial girdle. The other three are three-layer models consist of a vertical partial girdle in the center and a horizontal partial girdle in the top layer (Figure 7b), a horizontal partial girdle in the center and a horizontal cone in the top layer (Figure 7c), or a vertical thick girdle in the center and a tilted cone in the top layer (Figure 7d). The uncertainties on the model fabric parameters vary for the different models (Figure 8; Table S1). Generally, the azimuthal orientation of the fabric in the middle layer (domain 2 in Figure 7) is constrained best, while the opening angle of the vertical cone in the bottom domain (domain 1) has a higher uncertainty.

The anisotropy pattern and the 2' distribution that arises from the four best models is compared to results from SWS in Figure 9. Calculating SWS parameters for each event individually, best minimizes 2. E.g. Σ 2'=0.32 in the case of the input data used in inversion, as a highest quality subset from all SWS results was chosen. Nevertheless, all models obtained from the fabric inversion resample the main features described in Section 3.2, which feature a higher percentage of anisotropy for small incidence angles and an alternating pattern of smaller and larger V_S for larger incidence angles (Features f1/1x, f2 and f3/3x in Figure 4). However, only the fourth model can explain the asymmetry of the SWS data relative to ice flow direction (features f4/f4x and f1x, f2x in Figure 4). The recovery of these features mainly arises from the tilted cone fabric in the uppermost domain of the model (domain 3 in Figure 7d).

We apply sensitivity tests for the three three-layer models, aiming to determine the optimum depth of the domain boundaries and the significance of the vertical cone fabric (see details in Section 4.2). Results are illustrated in Figure 10. For all scenarios, the quality of the solution decreases, expressed by larger Σ 2' and Σerror values. This suggests that the initially defined domain depths, and a vertical cone fabric in the lowest domain represent a model configuration closest to the true situation. Furthermore, these tests show that the order of the depth layers is not exchangeable. This is expected as the waveforms are sequentially modulated along the ray path.

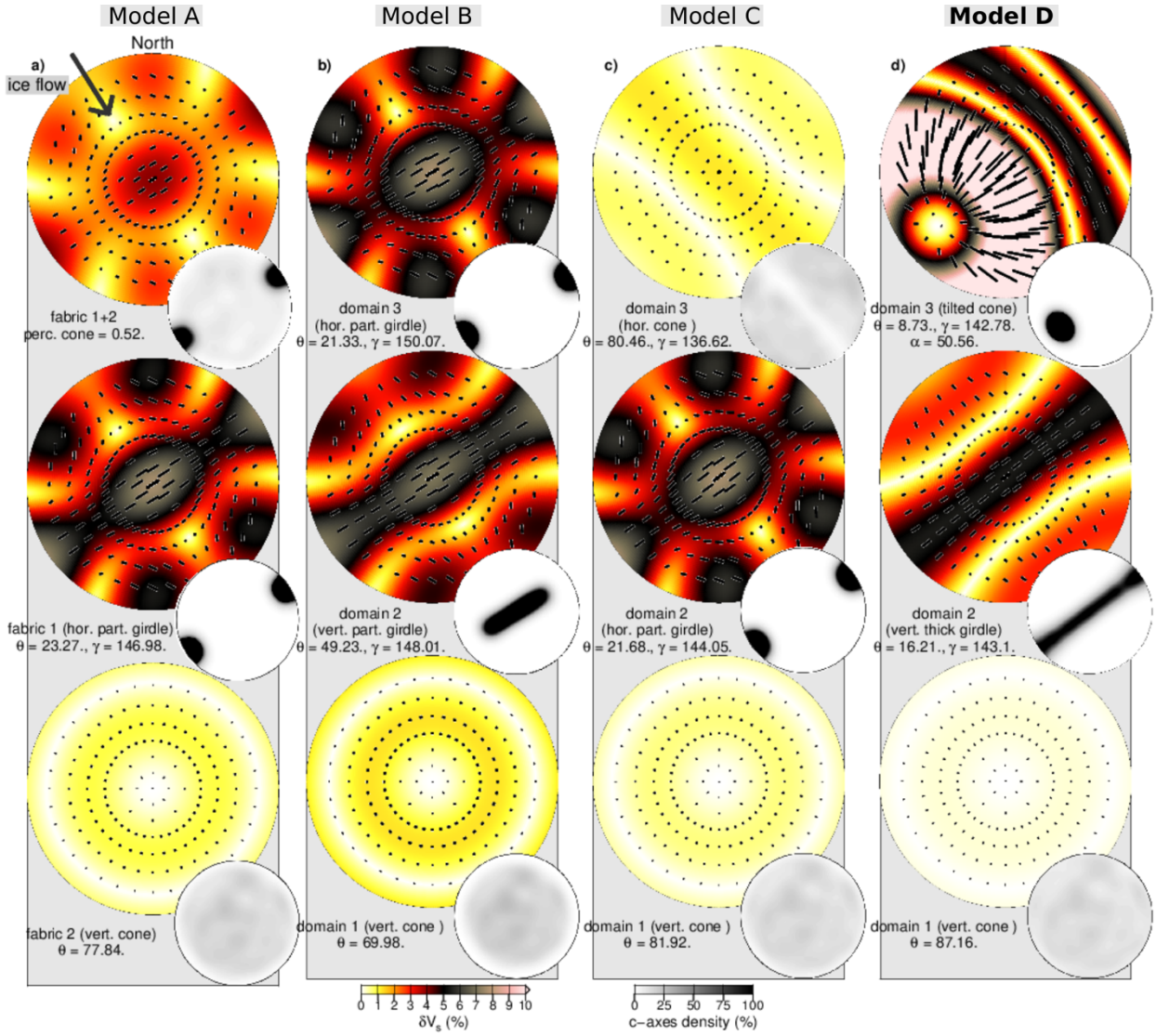

Figure 7: Inversion results for each depth domain and fabric type from the four best models as upper hemisphere plots. The associated coordinate system is plotted in Figure 1. Ice flow direction of RIS is highlighted as black arrow. Note that the incidence angles here refer to those of the rays in ice, which are less steep than those at the surface. This notation is chosen when visualizing the inversion results as the largest part of the ray paths is through the ice layer. Insets show associated c-axes distribution in gray scale. a) Results from 'mixed' fabric inversion. The top panel shows the SWS pattern obtained from combining the two fabrics, using Voigt-Reuss-Hill averaging. b-d) Results from three-layer inversion. Each polar plot represents results from one depth layer. See Table S1

and Figure 8 for the uncertainty ranges of the parameters. As argued in Section 5.2, we consider Model D as the most likely.

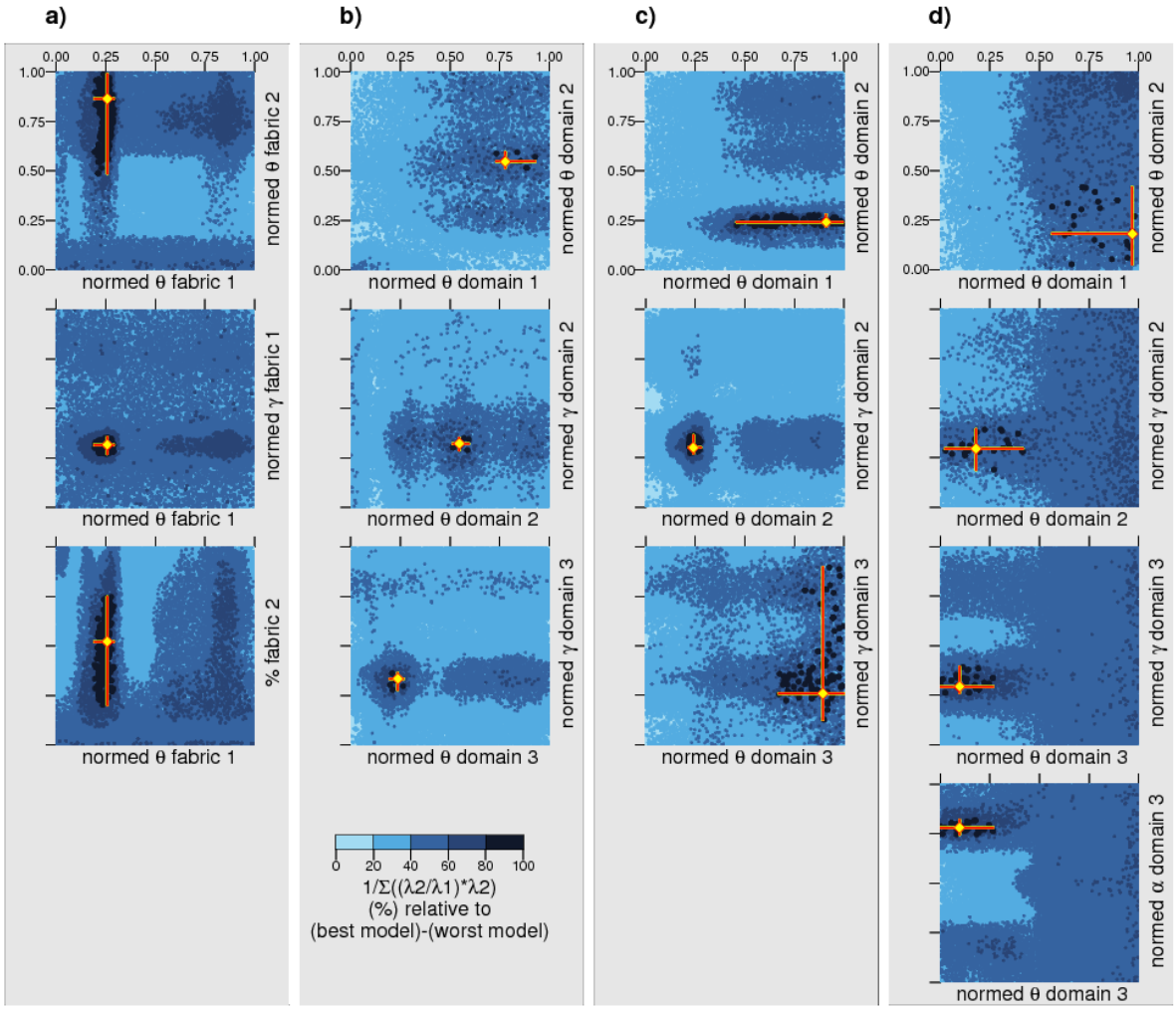

Figure 8: Uncertainty of model parameters for the four models presented in Figure 7. All parameters are normed to the range from 0 to 1. See Table S1 for the values in degrees and Figure 1 for the coordinate system used. a) 'mixed' model as presented in Figure 7a. Fabric 1 is a horizontal partial girdle, fabric 2 a cone. b-d) 3-layer models as presented in Figures 7 b-d.

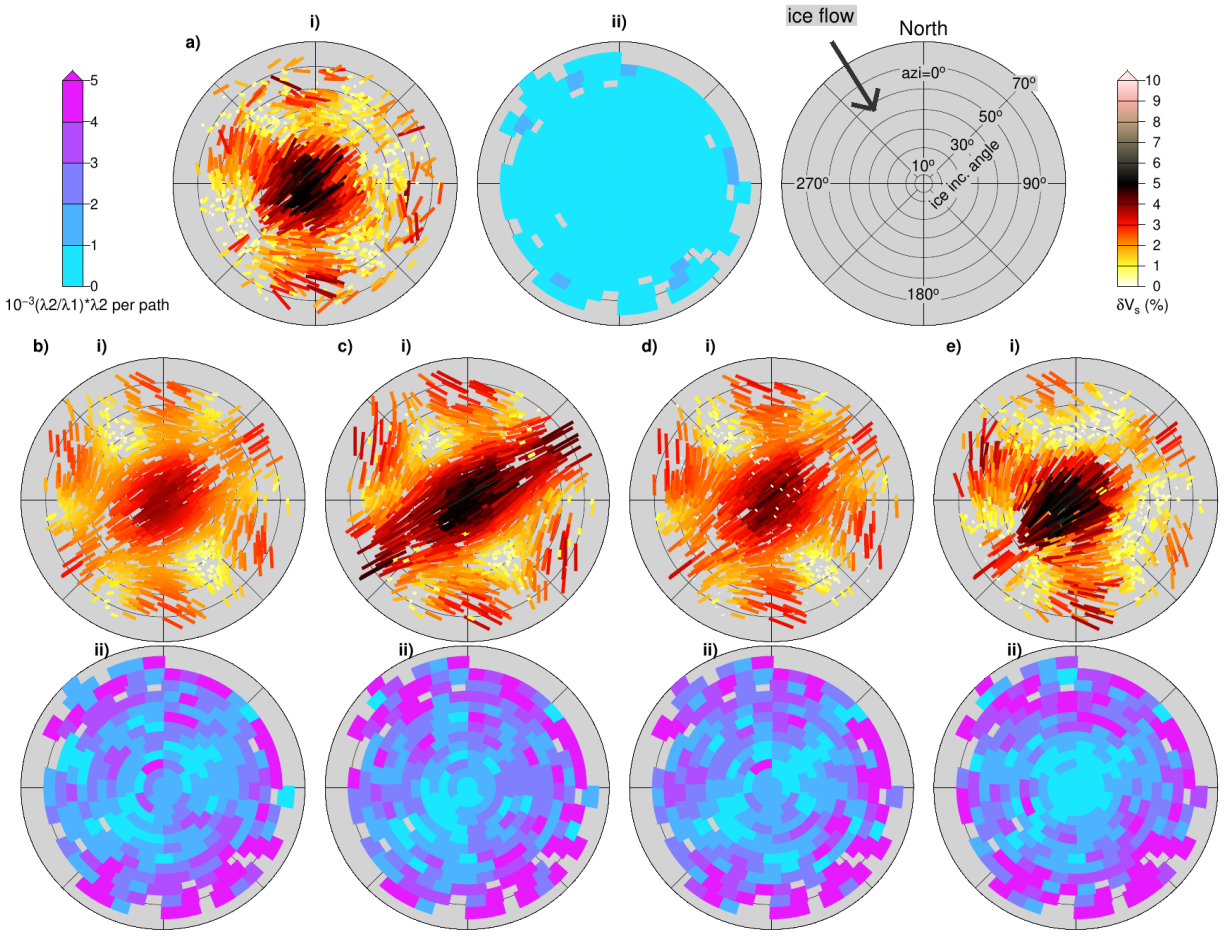

Figure 9: Inversion results from the four best models, compared to SWS results from shear wave splitting. Subfigures i show an upper hemisphere plot of SWS parameters for each ray (azi=0° corresponds to North; ice flow direction at RIS is highlighted with a black arrow), while subfigures ii show 2', averaged in bins, similar to Figure 5. a) SWS parameters and 2' from SWS of individual rays (Σ 2' = 0.32). b-e) SWS parameters and 2' from inversion for ice fabric. Details of the inversion results are listed in Table S1 and visualized in Figures 7 and 8. b) Results from the inversion for a combination of a vertical cone and a horizontal partial girdle (Σ 2' = 2.72). c) Results from a three-layer inversion with a vertical cone at the base, a vertical partial girdle in the center and a horizontal partial girdle in the top layer (Σ 2' = 2.81). d) Results from a three-layer inversion with a vertical cone at the base, a horizontal partial girdle in the center and a horizontal cone in the top layer (Σ 2' = 2.74). e) Results from a three-layer inversion with a vertical cone at the base, a vertical thick girdle in the center and a tilted cone in the top layer (Σ 2' = 2.80).

5 Discussion and Interpretation

5.1 Unambiguously constrained fabric components

Although composed of different fabric types, the four models with statistically comparable fits (Figure 7) share several similarities: First, the vertical cone, which was predefined in the lowermost model layer, or as one fabric component of the 'mixed' model, has a wide opening angle (>70°) in all four models. Second, the fabrics in the middle and top layers, or the second fabric component in the 'mixed' model, are oriented approximately perpendicular to ice flow direction. Lastly, the fabric in the middle layer, or the second component in the 'mixed' model, features largest V_S in a band perpendicular to ice flow. It is due to the characteristics of the observed SWS pattern (Figures 4 and 5) and due to the anisotropy characteristics of the different ice fabrics that multiple combinations are numerically comparable. Nevertheless, the inversion revealed that a basal broad cone fabric in combination with a fabric, which features the elements described above, is essential to explain the SWS pattern below RIS.

In addition, the inversion unambiguously allows us to exclude several scenarios. First, it is unlikely that a horizontal cone fabric (see Figure 5a) exists in the central layer. Such a fabric features a too small anisotropy percentage perpendicular to flow and at small incidence angles and is therefore not compatible with the SWS data. This is an important contribution in addition to results from radar surveys, as such data cannot discriminate between a horizontal cone or a vertical thick girdle fabric. The sensitivity analysis showed that placing a vertical cone fabric in the central layer, or excluding the vertical cone from the inversion, increased Σ 2'. Thus, also the sensitivity analysis emphasizes that a vertical cone fabric at the base of RIS is an essential element, independent of which of the models shown in Figure 7 is chosen. In addition, the sensitivity analysis (Figure 10) showed that the input geometry initially defined yielded the best results. This illustrates that using radar results to define the input model geometry is a valid and important tool when inverting SWS data for ice fabric.

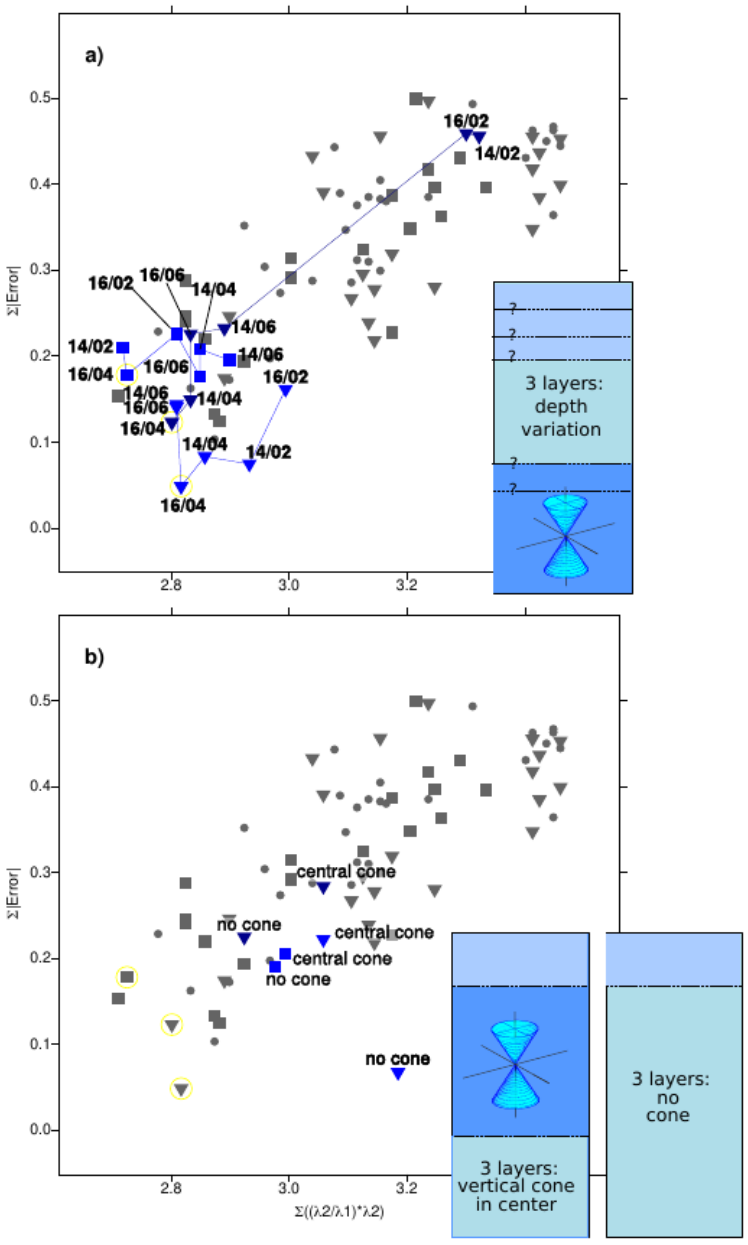

Figure 10: Sensitivity analysis, testing further model geometries with the three best three-layer models presented in Figures 7-9. Color coded symbols are inversion results in the same nomenclature than used in Figure 6. Gray symbols in the background are model results as presented in Figure 6 for orientation. a) The depth of the domain boundaries is varied. Values on top of the symbols indicate

the depths of the two domain boundaries: For instance, 16/02 corresponds to a boundary of domain 1 at 1600 m depth and a boundary of domain 2 at 200 m depth. The thin lines connect model with the same fabric. b) The significance of including a vertical cone fabric is tested. In the 'central cone' models, a vertical cone fabric is predefined in the depth range between 400 and 1600 m depth. In the 'no cone' models, the domain with the vertical cone is removed and the input models consist of two depth domains (0-400 m depth and 400-2200 m depth) only.

5.2 Three-layer model with vertical thick girdle fabric in central layer (Model D) as preferred solution

Despite the fact that there are several different models with statistically comparable fits, we favor the fourth model (Model D; Figure 7d). This model features three depth layers and a vertical thick girdle fabric in its middle layer: One of the four best models is a 'mixed' fabric (Figure 7a), for which no layering is assigned, and a uniform ice fabric consisting of two fabric types combined throughout the entire ice column was assumed. The parameters we derive for this model are similar to the preferred model of Smith et al. (2017) (Θ cone = 73°; Θ hor. partial girdle = 22°; = 144°; mixing percentage = 53 % vs here: Θ cone = 78°; Θ hor. partial girdle = 23°; = 147°; mixing percentage = 52 %). This consistency validates the inversion approach chosen here. However, we nevertheless argue that the 'mixed' model is unlikely to represent the true ice fabric of RIS. First, the 'mixed' model is hard to explain physically. A distinct deformation regime results in a specific ice fabric. Therefore, and as also noted by Smith et al. (2017), the 'mixed' model rather suggests that the two fabric types exist within the ice but with their depth distribution previously unresolved. Second, radar imaging (T. M. Jordan, 2022) clearly shows that multiple layers of distinct ice fabric exist at RIS, which is incompatible with a uniform ice fabric. Lastly, the horizontal partial girdle fabric has not yet been observed in ice cores, potentially suggesting that it is less prevalent than other ice fabric types. Combining these arguments, we prefer to rule out the 'mixed' model as a likely candidate. The reason this model yields results comparable to the three-layer model is the specific fabric combination, with the broad cone modifying the waveforms little.

The two three-layer models, which feature a horizontal or vertical partial girdle fabric in the central layer (Figures 7b and 7c) also seem problematic. Although these models are compatible with results from radar, they also feature an ice fabric type as main contribution that has not been observed elsewhere. In addition, and possibly more importantly, these models do not reproduce the distinct asymmetry relative to ice flow, observed from the SWS data (features f1/f3/f4 versus f1x/f3x/f4x in Figure 4) and also overestimate the flow perpendicular anisotropy at incidence angles greater than 30° degrees (features f4/f4x in Figure 4).

Only model D (Figure 7d) is comparable with radar results. It is composed of fabric elements that are commonly observed in ice cores and captures the asym-

metry in the SWS data relative to ice flow direction. The latter is mostly due to the tilted cone fabric in the uppermost layer. Potentially, the flow-perpendicular asymmetry in the SWS dataset could be caused by spatially variable fabric beneath our network. However, we consider this scenario as unlikely as we did not find a clear signal of spatial variable fabric in the SWS data (see Supplementary Text 1). In addition, the SWS patterns from the different spatial domains, which we used to generate the input for inversion, reveal the asymmetry as well (Figure S6). These different elements make us conclude that the fourth model of Figure 7 likely represents the true situation at RIS best.

As only the fourth model shown in Figure 7 captures the flow-perpendicular asymmetry in the data, one might argue that Σ 2' is not the ideal measure to characterize the quality of the inversion results. We experimented with using 2 instead but found that this destabilized the inversion in a way that it was more difficult for the algorithm to find a global maximum. We further refrained from using any weighting function, e.g., weighting input data with smaller split times differently, as this would introduce a bias in the input data. The input waveforms were chosen based on distinct quality criteria and an equal distribution of the input data with regards to azimuth and incidence angle was guaranteed. Thus, this analysis shows that it is due to the specific geometry of the anisotropy pattern that the results from one 'mixed' and from three three-layer models appear equally good. However, as argued above, we are confident that the inversion, together with additional information from other studies, allows us to put forward model D (Figure 7d) as the most likely.

5.3 Impact of preferred Solution (Model D) on Mechanical Properties

To show the impact of our fabric solution in ice flow we estimate the ice viscosity tensor, which is an important parameter in flow-laws for ice sheet models. We follow the method of Jordan et al. (2022) where the c-axis orientation distribution is represented with a second-order orientation tensor. The eigenvalues of this tensor represent the relative c-axis concentration along the principal coordinates. Unlike with downward-looking radar methods, which are limited to measuring the orientation of the horizontal eigenvectors and their relative strength, the results from the SWS inversion allow us to estimate the amplitude and orientation of all three eigenvectors in the principal axes. We then follow the scheme of Jordan et al. (2022) to derive the viscosity enhancement due to fabric to understand the effects of the measured fabric on viscosity and deformation.

Figure 11a presents the eigenvalue representation of the four best fit models described above. To allow direct comparison with existing downward-looking radar observations we represent the orientation tensor in natural flow coordinates, where t represents the horizontal direction of ice flow, n is normal to flow and also in the horizontal and z is the vertical. Under the assumption that the vertical is a principal vector, the orientation tensor can be represented by the difference in horizontal eigenvalues (Δa), azimuth of the fabric with respect to the direction of flow ( ) and the vertical component of the orientation tensor

(a_z) (Jordan et al, 2022). This representation clearly emphasizes the differences between the four models albeit the SWS patterns appear similar.

One of the main strengths of SWS when compared with downward-looking radar, is that it provides information of the fabric in all directions. Jordan et al (2022) highlights how the lack of information of the vertical component of the fabric ($0<a_z<1-\Delta a$) translate into a large uncertainty on ice properties for fast-flowing ice.

Ice viscosity often is divided in an isotropic component, related to the ice flow law, and an anisotropic component, related to ice fabric (Ma et al., 2010; Martín et al., 2009). We use GOLF anisotropic flow law (Gillet-Chaulet, 2006) from the ElmerIce AIFlow solver (Gagliardini et al., 2013) to calculate the latter. The solver searches viscosity for a given second-order orientation tensor, in a space that has been tabulated using different viscosity models and crystal-scale parameters. Following Jordan et al (2022), we assume that = 0.04, the ratio of viscosity of the grain for shear parallel to the basal plane to that in the basal plane; = 1, the ratio of the viscosity in compression or tension along the c-axis to that in the basal plane; and the model used for tabulation is a viscoplastic self-consistent model.

Figure 11b then presents the derived viscosity enhancement factors due to fabric for the most representative components for our preferred model. Values greater than one represent stiffening or hardening to strain and values lower than one softening. In the shallowest layer we see a complex range of softening and hardening, with the most significant effects on $_{\text{nznz}}$ (hardening to vertical shear perpendicular to flow), $_{\text{tntn}}$ (hardening to lateral shear), and $_{\text{tztz}}$ (hardening to vertical shear parallel to flow). However, the bulk of the ice column, in the middle layer, exhibits hardening to compression or extension along flow with an enhancement factor of $_{\text{tttt}} = 2.16$, which equates to a factor of 10 in viscosity due to the third power if, as commonly assumed, we use 3 for the rheological index in Glen's flow law (Ma et al., 2010; Martín et al., 2009). Also, in the middle layer, ice is 3.5 times softer to compress or extend across flow than along flow [$(_{\text{tttt}}/_{\text{nnnn}})^3$=3.5] and 16 times softer to shear than to compress or extend along flow [$(_{\text{ttt}}t/_{\text{tztz}})^3$=16]. We see little effect in the deepest layer of the ice column. This shows that the character of ice deformation not only dependents on the direction of applied force, but also on the depth within the ice column.

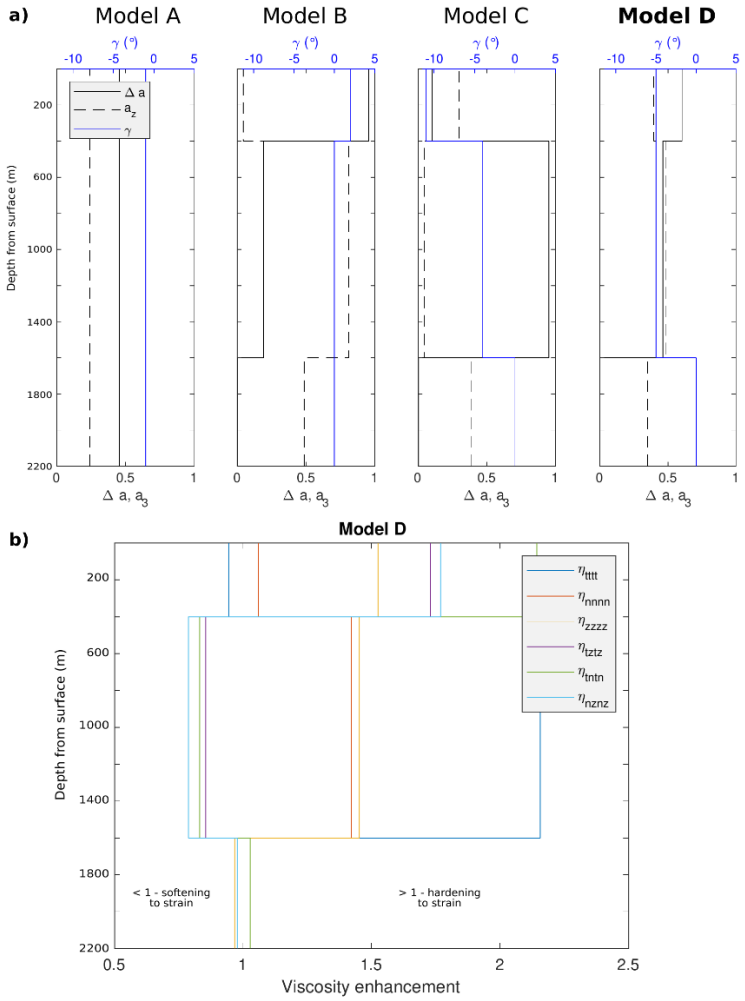

Figure 11: a) Fabric orientation tensor for the four models shown in Figures 7-9. Tensors are represented as difference between the horizontal eigenvalues (Δa), the horizontal azimuth with respect to the flow direction ( ), and the vertical eigenvalue (a_z). Δa and can be measured from downward-looking radar, whereas a_z can not be measured. Model labels as in Figure 7. b) Principal components of the viscosity enhancement tensor for model D (Fig. 7d), highlighting that viscosity strongly depends on the component of deformation. As Jordan et al (2022) we use a natural flow frame of reference: t represents tangential to flow, n normal to flow and z is the vertical.

5.4 Formation Scenario for preferred Ice Fabric (Model D)

Ice fabric at a specific location is a combination of the strain history and recrystallization processes (Alley, 1988). Ice fabric is not instantaneously developed

and our results thus point to a complex strain history of RIS. Here, we discuss potential formation mechanisms for an ice fabric as resolved in Model D (Figure 7d).

In the upper 400 m layer a tilted cone fabric is observed. We suggest that this measured fabric results from complexity in the shallow ice column that is 'averaged' by the SWS method. Radar measurements show a complex finer scale depth structure near the surface of RIS (T. M. Jordan, 2022) but are insensitive to azimuthal variations in fabric such as this tilted fabric. SWS is insensitive to a layering on the order of meters and such features may be reflected in a bulk anisotropic medium with a tilted symmetry axis.

In the middle layer the measured fabric is dominated by a thick vertical girdle, oriented perpendicular to flow. This is consistent with the surface strain measured upstream of our study region which is dominated by along flow extension at the surface (Jordan et al., 2022), and could result this fabric geometry. It is therefore likely that the fabric measured here in the middle layer was formed by extensional flow upstream of the current location, and subsequently buried and advected to the experiment site.

Our results suggest that a vertical cone fabric dominates the deepest layer. There are two possible formation mechanisms for this fabric. A vertical cone can develop where basal shear dominates over basal sliding. In the extreme scenario, where ice is stagnant, the main component of strain will be vertical compaction, again resulting in a vertical cone fabric. Alternatively, the fabric may form by ice recrystallization, erasing an older fabric and making the fabric less dependent on flow-induced development (Alley, 1992). At RIS, large number of icequakes are observed at the ice-bed interface (Kufner et al., 2021; E. C. Smith et al., 2015) indicating that basal sliding dominates over basal shear, and it is likely that a similar regime existed in the past (Gudmundsson & Jenkins, 2009). Ice recrystallization is therefore the more likely fabric formation process. The sharp change in ice fabric between the lower and middle layers may reflect a change in crystal size. Larger grain sizes enhance recrystallization (Alley, 1992), and this sharp transition potentially reflects a change in the dominant grain size due to a different climate at the time of formation.

As noted in Section 4.2, our method resolves only large scale characteristics (i.e., >200 m thickness) of the ice in the anisotropy-intensity range considered here. This is mainly due to the uncertainty in the SWS measurements. Therefore, we cannot rule out a thin layer of ice (e.g., several meters) at the base of RIS with a fabric different from the vertical cone. Similarly, the uppermost layer discussed here includes the firn (upper ~100 m), which is likely less anisotropic than the ice below it (E. C. Smith et al., 2017).

Interestingly, the ice fabric we infer for the bottom part of RIS is very similar to that observed for the entire ice column below the firn at Whillans Ice Stream using active seismic imaging (Picotti et al. (2015)). They suggested that ice fabric formation is dominated by vertical compression rather than in-

ternal extensional deformation. However, Picotti et al. (2015) note that the ice fabric further upstream might be a vertical girdle, which is erased at their study side. In contrast to Whillans Ice Stream, our analysis at RIS shows the basal cone layer to be overlain by an ice layer with a different fabric that testifies to dominantly along-flow extension. Potentially, multiple layers of different ice fabric could evolve at RIS due to its larger ice mass (RIS is much thicker than Whillans Ice Stream; ~780 m versus ~2200 m at RIS). Alternatively, these observations might emphasize that the ice fabric along the length of an ice stream is highly variable due to both, strain history and recrystallization. This would imply that multiple fabric studies along the length of an ice stream are needed to understand its current deformation.

6 Summary and Conclusions

We present more than 200,000 shear-wave splitting measurements from Rutford Ice Stream, a fast flowing (>1 m/day), ~2.2 km thick West Antarctic Ice Stream. Results indicate seismic anisotropy of up to 6.6% in the glacial ice. Anisotropy varies, however, depending on azimuth and incidence angle of the seismic rays. These variations are much stronger than temporal or spatial variations in the SWS pattern.

We invert the data for depth-dependent ice fabric, making use of the fact that different types of ice fabric can be discriminated against each other based on their anisotropic pattern. The layout of the input models for inversion is designed based on prior information derived from radar studies (T. M. Jordan, 2022). The inversion shows that the SWS pattern is equally well explained by four different models. One of the models is a combination of a vertical cone fabric and a horizontal partial girdle fabric. The other models feature three layers of different ice fabric with the deepest layer (500 m thickness) being a vertical cone fabric with wide (>70°) opening angle. One model then consists of a horizontal partial girdle in the middle layer (1200 m thickness) and a horizontal cone in the uppermost layer (400 m thickness). The next model features a vertical partial girdle (middle) and a horizontal girdle (top). The last model features a vertical girdle (middle) and a tilted cone (top). As only the last model (Model D in Fig. 7). reproduces a distinct asymmetry of the seismic anisotropy relative to ice flow, which can be seen in the SWS results, we favor this model as the most realistic.

Such a fabric could arise from mostly vertical compression due to high basal shear at the base of the ice stream or due to recrystallization of the ice in the basal unit. The middle and upper layer could arise from mostly extension along flow at central depths and a mixture of horizontal shearing across flow and compression near the surface. We suggest that such a scenario might have formed from a combination of past and current deformation under different stress regimes, likely in combination with ice recrystallization.

We calculate the viscosity enhancement factor for the preferred ice fabric model and find that the middle layer is significantly (3.5 times) harder to deform

along flow than across flow. By contrast, there is little directional effect in the lowermost layer. Thus, a single enhancement factor for the entire depth range of the ice column, as often used in ice sheet models, is unlikely to represent the results gained here. It remains a topic of future research if SWS splitting at RIS is representative for fast-flowing ice streams in general or if the observed pattern is dominantly influenced through local factors.

This study shows that passive seismic imaging can help to constrain ice fabric at far lower cost than through direct measurements (e.g. boreholes), if prior knowledge of the depth structure of the ice is available. Furthermore, results from SWS complement other passive geophysical methods like radar imaging, as the ice fabric in all three dimensions can be constrained.

Acknowledgments

This work was funded by NERC AFI award numbers NE/G014159/1 and NE/G013187/1. The authors thank the staff at Rothera Research Station and BAS logistics for enabling the fieldwork associated with this project and the BEAMISH field team (2018/2019) for acquiring the passive seismic data. Seismic instruments were provided by NERC SEIS-UK (Loan 1017), by BAS and by the Incorporated Research Institutions for Seismology (IRIS) through the PASSCAL Instrument Center at New Mexico Tech. The facilities of the IRIS Consortium are supported by the National Science Foundation's Seismological Facilities for the Advancement of Geoscience (SAGE) Award under Cooperative Support Agreement EAR-1851048.

Open Research

Data: Waveform data and SWS results (Kufner et al., 2022) can be accessed via the Polar Data Center (the password protection will be lifted once this manuscript is published):

The dataset can be accessed directly via this URL:

https://ramadda.data.bas.ac.uk/repository/entry/show?entryid=6fcc17ad-425b-4367-bd23-c4133a38e359

Reviewer access instructions are available at this URL:

https://www.bas.ac.uk/data/uk-pdc/reviewer-access/

Software: Version 2.2 of MFAST used for shear wave splitting analysis is available via https://mfast-package.geo.vuw.ac.nz/. The software used for ice fabric inversion is still under development the authors of this manuscript can be contacted via mail for requests.

References

Adalgeirsdóttir, G., Smith, A. M., Murray, T., King, M. A., Makinson, K., Nicholls, K. W., & Behar, A. E. (2008). Tidal influence on Rutford

Ice Stream, West Antarctica: Observations of surface flow and basal processes from closely spaced GPS and passive seismic stations. *Journal of Glaciology*. https://doi.org/10.3189/002214308786570872Alley, R. B. (1988). Fabrics in polar ice sheets: Development and prediction. *Science*, *240*(4851). https://doi.org/10.1126/science.240.4851.493Alley, R. B. (1992). Flow-law hypotheses for ice-sheet modeling. *Journal of Glaciology*, *38*(129). https://doi.org/10.1017/S0022143000003658Azuma, N., & Goto-Azuma, K. (1996). An anisotropic flow law for ice-sheet ice and its implications. *Annals of Glaciology*, *23*. https://doi.org/10.3189/s0260305500013458Budd, W. F., Warner, R. C., Jacka, T. H., Li, J., & Treverrow, A. (2013). Ice flow relations for stress and strain-rate components from combined shear and compression laboratory experiments. *Journal of Glaciology*, *59*(214). https://doi.org/10.3189/2013JoG12J106Crampin, S., & Lovell, J. H. (1991). A decade of shear-wave splitting in the Earth's crust: what does it mean? what use can we make of it? and what should we do next? *Geophysical Journal International*, *107*(3). https://doi.org/10.1111/j.1365-246X.1991.tb01401.xDuval, P., Ashby, M. F., & Anderman, I. (1983). Rate-controlling processes in the creep of polycrystalline ice. *Journal of Physical Chemistry*, *87*(21). https://doi.org/10.1021/j100244a014Faria, S. H., Weikusat, I., & Azuma, N. (2014a). The microstructure of polar ice. Part I: Highlights from ice core research. In *Journal of Structural Geology*. https://doi.org/10.1016/j.jsg.2013.09.010Faria, S. H., Weikusat, I., & Azuma, N. (2014b). The microstructure of polar ice. Part II: State of the art. In *Journal of Structural Geology* (Vol. 61). https://doi.org/10.1016/j.jsg.2013.11.003Gagliardini, O., Gillet-Chaulet, F., & Montagnat, M. (2009). A review of anisotropic polar ice models: from crystal to ice-sheet flow models. *Low Temperature Science*, *68*(January).Gagliardini, O., Zwinger, T., Gillet-Chaulet, F., Durand, G., Favier, L., De Fleurian, B., Greve, R., Malinen, M., Martín, C., Räback, P., Ruokolainen, J., Sacchettini, M., Schäfer, M., Seddik, H., & Thies, J. (2013). Capabilities and performance of Elmer/Ice, a new-generation ice sheet model. *Geoscientific Model Development*, *6*(4). https://doi.org/10.5194/gmd-6-1299-2013Gillet-Chaulet, F. (2006). Flow-induced anisotropy in polar ice and related ice-sheet flow modelling. *Journal of Non-Newtonian Fluid Mechanics*, *134*(1-3 SPEC. ISS.). https://doi.org/10.1016/j.jnnfm.2005.11.005Graham, F. S., Morlighem, M., Warner, R. C., & Treverrow, A. (2018). Implementing an empirical scalar constitutive relation for ice with flow-induced polycrystalline anisotropy in large-scale ice sheet models. *Cryosphere*, *12*(3). https://doi.org/10.5194/tc-12-1047-2018Gudmundsson, G. H., & Jenkins, A. (2009). Ice-flow velocities on Rutford Ice Stream, West Antarctica, are stable over decadal timescales. *Journal of Glaciology*, *55*(190). https://doi.org/10.3189/002214309788608697IPCC. (2007). Climate Change 2007: Synthesis report Summary for Policymakers. *Hemisphere*, *335*(November).Jordan, T. M., Martín, C., Brisbourne, A. M., Schroeder, D. M., & Smith, A. M. (2022). Radar Characterization of Ice Crystal Orientation Fabric and Anisotropic Viscosity Within an Antarctic Ice Stream. *Journal of Geophysical Research: Earth Surface*, *127*(6).

https://doi.org/10.1029/2022JF006673King, E. C., Pritchard, H. D., & Smith, A. M. (2016). Subglacial landforms beneath Rutford Ice Stream, Antarctica: detailed bed topography from ice-penetrating radar. *Earth System Science Data*. https://doi.org/10.5194/essd-8-151-2016Kufner, S. K., Brisbourne, A. M., Smith, A. M., Hudson, T. S., Murray, T., Schlegel, R., Kendall, J. M., Anandakrishnan, S., & Lee, I. (2021). Not all Icequakes are Created Equal: Basal Icequakes Suggest Diverse Bed Deformation Mechanisms at Rutford Ice Stream, West Antarctica. *Journal of Geophysical Research: Earth Surface*, *126*(3). https://doi.org/10.1029/2020JF006001Kufner, S. K., Brisbourne, A., Smith, A., Wookey, J., Martin, C., Hudson, T., & Kendall, J. M. (2022). Shear wave splitting catalogue, Rutford Ice Stream (West Antarctica), November 2018 to February 2019 (Version 1.0). *NERC EDS UK Polar Data Centre*. https://doi.org/https://doi.org/10.5285/6FCC17AD-425B-4367-BD23-C4133A38E359Lutz, F., Eccles, J., Prior, D. J., Craw, L., Fan, S., Hulbe, C., Forbes, M., Still, H., Pyne, A., & Mandeno, D. (2020). Constraining Ice Shelf Anisotropy Using Shear Wave Splitting Measurements from Active-Source Borehole Seismics. *Journal of Geophysical Research: Earth Surface*, *125*(9). https://doi.org/10.1029/2020JF005707Ma, Y., Gagliardini, O., Ritz, C., Gillet-Chaulet, F., Durand, G., & Montagnat, M. (2010). Enhancement factors for grounded ice and ice shelves inferred from an anisotropic ice-flow model. *Journal of Glaciology*, *56*(199). https://doi.org/10.3189/002214310794457209Martín, C., Gudmundsson, G. H., Pritchard, H. D., & Gagliardini, O. (2009). On the effects of anisotropic rheology on ice flow, internal structure, and the age-depth relationship at ice divides. *Journal of Geophysical Research: Earth Surface*, *114*(4). https://doi.org/10.1029/2008JF001204Maurel, A., Lund, F., & Montagnat, M. (2015). Propagation of elastic waves through textured polycrystals: Application to ice. *Proceedings of the Royal Society A: Mathematical, Physical and Engineering Sciences*. https://doi.org/10.1098/rspa.2014.0988Paulssen, H. (2004). Crustal anisotropy in southern California from local earthquake data. *Geophysical Research Letters*, *31*(1). https://doi.org/10.1029/2003GL018654Picotti, S., Vuan, A., Carcione, J. M., Horgan, H. J., & Anandakrishnan, S. (2015). Anisotropy and crystalline fabric of whillans ice stream (West Antarctica) inferred frommulticomponent seismic data. *Journal of Geophysical Research: Solid Earth*, *120*(6). https://doi.org/10.1002/2014JB011591Savage, M. K., Wessel, A., Teanby, N. A., & Hurst, A. W. (2010). Automatic measurement of shear wave splitting and applications to time varying anisotropy at Mount Ruapehu volcano, New Zealand. *Journal of Geophysical Research: Solid Earth*, *115*(12). https://doi.org/10.1029/2010JB007722Savage, M. S. (1999). Seismic anisotropy and mantle deformation: What have we learned from shear wave splitting? *Reviews of Geophysics*, *37*(1). https://doi.org/10.1029/98RG02075Silver, P. G., & Chan, W. W. (1991). Shear wave splitting and subcontinental mantle deformation. *Journal of Geophysical Research*, *96*(B10). https://doi.org/10.1029/91jb00899Silver, P. G., & Savage, M. K. (1994). The Interpretation of Shear-Wave Splitting Parameters In the Presence of Two Anisotropic Layers. *Geophysical Journal In-*

ternational, *119*(3). https://doi.org/10.1111/j.1365-246X.1994.tb04027.xSmith, A. M., Anker, P. G. D., Nicholls, K. W., Makinson, K., Murray, T., Costas-Rios, S., Brisbourne, A. M., Hodgson, D. A., Schlegel, R., & Anandkrishnan, S. (2020). Ice stream subglacial access for ice sheet history and fast ice flow: The BEAMISH Project on Rutford Ice Stream, West Antarctica and initial results on basal conditions. *Annals of Glaciology*, 1–9. https://doi.org/10.1017/aog.2020.82Smith, E. C., Baird, A. F., Kendall, J. M., Martín, C., White, R. S., Brisbourne, A. M., & Smith, A. M. (2017). Ice fabric in an Antarctic ice stream interpreted from seismic anisotropy. *Geophysical Research Letters*. https://doi.org/10.1002/2016GL072093Smith, E. C., Smith, A. M., White, R. S., Brisbourne, A. M., & Pritchard, H. D. (2015). Mapping the ice-bed interface characteristics of Rutford Ice Stream, West Antarctica, using microseismicity. *Journal of Geophysical Research F: Earth Surface*. https://doi.org/10.1002/2015JF003587T. M. Jordan, C. M. A. M. B. D. M. S. A. M. S. (2022). Radar characterization of ice crystal orientation fabric and anisotropic rheology within an Antarctic ice stream. *Submitted to JGR: Earth Surface* .Teanby, N. A., Kendall, J. M., & van der Baan, M. (2004). Automation of shear-wave splitting measurements using cluster analysis. *Bulletin of the Seismological Society of America*, *94*(2). https://doi.org/10.1785/0120030123Walsh, E., Arnold, R., & Savage, M. K. (2013). Silver and Chan revisited. *Journal of Geophysical Research: Solid Earth*, *118*(10). https://doi.org/10.1002/jgrb.50386Wookey, J. (2012). Direct probabilistic inversion of shear wave data for seismic anisotropy. *Geophysical Journal International*, *189*(2). https://doi.org/10.1111/j.1365-246X.2012.05405.x